applied sciences

MDPI

Article

Method to Reverse-Engineer Head Impact Conditions Leading to a Traumatic Brain Injury by Combining MRI Images and a Finite Element Model of the Head and Brain

Thais Manlius [1,2], Pierre Simeone [3,4,†], Clémence Delteil [5,6,†], Véronique Bouvette [2,7,8], Cyrile Duquenoy [1], Jean-Louis Milan [1], Yves Godio-Raboutet [1], Louis Puybasset [9,10], Éric Wagnac [2,4,5], Lionel Thollon [1,2] and Nicolas Bailly [1,2,*]

1 Laboratoire de Biomécanique Appliquée, Aix-Marseille Université, Université Gustave Eiffel, 13015 Marseille, France
2 iLab-Spine: International Laboratory on Spine Imaging and Biomechanics, 13015 Marseille, France
3 Department of Anesthesiology and Critical Care Medicine, AP-HM, University Hospital Timone, Aix Marseille University, 13005 Marseille, France
4 Timone Neuroscience Institute, CNRS, Aix Marseille University, 13005 Marseille, France
5 Institut Médico-Légal, Hôpital de la Timone, Marseille University Hospital, 264 rue St-Pierre, 13005 Marseille, France
6 CNRS, EFS, ADES, Aix Marseille University, 13015 Marseille, France
7 Department of Mechanical Engineering, École de Technologie Supérieure, 1100 Rue Notre-Dame Ouest, Montréal, QC H3C 1K3, Canada
8 Research Center, CIUSSS du Nord-de-l'île-de-Montréal, 5400 Boul Gouin O, Montréal, QC H4J 1C5, Canada
9 Department of Anesthesiology and Critical Care Medicine, Sorbonne Université, AP-HP, Pitié-Salpêtrière Hospital, 75006 Paris, France
10 Laboratoire d'Imagerie Biomédicale, Sorbonne Université, CNRS, INSERM, 75006 Paris, France
* Correspondence: nicolas.bailly@univ-eiffel.fr
† These authors contributed equally to this work.

Abstract

Reconstructing traumatic brain injury loading conditions remains challenging in forensic biomechanics. This study presents a proof-of-concept inverse-analysis framework for identifying plausible head impacts from post-traumatic brain imaging. It was applied to a pedestrian struck by a car who sustained severe brain injury and a malar fracture. Cerebral microbleeds on T1-weighted MRI and regions of abnormal fractional anisotropy on diffusion tensor imaging served as injury markers. A partially personalized finite element head model was subjected to 120 impacts compatible with the facial fracture, varying velocity, orientation, and contact surface. Predicted regions of elevated maximum principal strain (>0.2) were compared with observed injury locations using the Matthews correlation coefficient (MCC). With T1-weighted lesions alone, the best simulation achieved an MCC of 0.11, with high specificity (0.84) but low sensitivity (0.50), reflecting the difficulty of reproducing sparse, dispersed microbleeds. Including regions of abnormal fractional anisotropy improved performance, yielding an MCC of 0.34 and a sensitivity of 0.884. The best scenarios involved impacts to the lower posterior maxillary region, near the mandible and zygomatic bone, at 4–7 m/s. These findings support lesion-informed inverse finite element modeling for forensic impact reconstruction and suggest that fractional anisotropy alterations may provide complementary information on brain deformation.

Keywords: traumatic brain injury; finite element head model; MRI; biomechanics; accident reconstruction

Check for updates

Academic Editor: Thomas Lindner

Received: 23 September 2026
Revised: 21 October 2026
Accepted: 27 October 2026
Published: 30 October 2026

Copyright: © 2026 by the authors. Licensee MDPI, Basel, Switzerland. This article is an open access article distributed under the terms and conditions of the Creative Commons Attribution (CC BY) license.

1. Introduction

Traumatic brain injury (TBI) is a major cause of death and disability worldwide, affecting millions of individuals each year. TBIs encompass a broad spectrum of neurological injuries, ranging from mild concussion to severe lesions [1]. They are commonly associated with road traffic accidents, falls, and sports-related impacts [2].

The type, location, and severity of brain injury strongly depend on the impact conditions [3]. Characterizing impact conditions is important for understanding injury mechanisms, supporting forensic investigations, and improving protective systems. Although the direct clinical management primarily relies on neurological examination and neuroimaging, a better understanding of impact biomechanics may also contribute to interpreting lesion patterns and refining prognostic assessment. A better understanding of the relationship between impact mechanics and brain injury could also help improve prevention strategies and clarify the biological mechanisms underlying primary and secondary damage [4].

In clinical practice, neuroimaging plays a central role in TBI assessment. In the acute phase, computed tomography (CT) is used to detect lesions such as skull fractures and intracranial hemorrhage, whereas magnetic resonance imaging (MRI) is more sensitive for identifying diffuse axonal injury, early ischemic changes, and other subtle lesions after the acute stage. Advanced MRI techniques, including diffusion-weighted imaging, diffusion tensor imaging, and MR spectroscopy, provide detailed information about brain structure, tissue integrity, and metabolism, and may contribute to long-term prognostic evaluation [5,6]. However, imaging remains primarily limited to the observation of post-traumatic lesions and provides limited direct information about the mechanical conditions that generated them.

Finite element (FE) models of the head and brain offer a promising way to bridge this gap. By estimating tissue-level responses such as strain, stress, and pressure during impact, these models help investigate injury mechanisms and support the evaluation of protective systems [4,7]. They are used to reconstruct real-world accidents, including vehicle collisions, sports impacts, and falls, and to compare simulated tissue responses with imaging or autopsy findings [8–14]. In this context, biomechanical metrics such as maximum principal strain or axonal strain are often used to identify regions at risk of injury. Over the past decades, FE head models have become increasingly sophisticated, incorporating detailed anatomy and advanced constitutive descriptions of brain tissue, including anisotropic and viscoelastic behavior [15–17]. They have also been validated against cadaveric experiments, intracranial pressure measurements, and brain motion data [18–20]. Nevertheless, important challenges remain. In particular, the relationship between simulated biomechanical responses and actual lesion patterns is still affected by uncertainties in accident reconstruction, injury thresholds, and inter-individual anatomical variability. Moreover, most available models remain generic and do not fully account for subject-specific brain geometry, which may limit injury prediction accuracy [9,21,22].

FE models are commonly used in a forward manner, that is, to predict tissue deformation and injury from known impact conditions [23,24]. In parallel, accident reconstruction approaches have mainly been employed to investigate head injury risk functions [25,26]. FE–based reconstructions have also been used in forensic contexts to test hypotheses, particularly regarding the mechanisms of skull fracture and the plausibility of specific impact scenarios as causes of brain injury [27–29]. However, to our knowledge, only a limited number of studies have explored the inverse approach namely, identifying the most plausible impact conditions based on observed brain injuries, such as those detected on MRI. It remains unclear whether the spatial distribution of traumatic lesions observed in post-traumatic imaging can be reliably used to infer the most probable impact scenario.

This study is therefore designed as a proof of concept for a reverse-engineering framework aimed at identifying likely head impact conditions from post-traumatic imaging data. The proposed approach combines advanced MRI post-processing pipeline to assess brain structure geometry and injured areas, partial geometric personalization of a subject-specific FE head model and a large design of experiments of FE impact reconstruction in which key impact parameters, including impact location, velocity, and contact surface, are systematically varied. Simulated brain tissue responses are then compared with lesions observed on CT and MRI in order to identify the impact conditions that best explain the imaging findings. Finally, a pipeline was developed to convert FE simulation results into MRI processing tool to enable clinicians to use this work for forensic applications.

2. Materials and Methods

The overall approach is summarized in Figure 1. The inputs consist of (1) general accident information, used to constrain the range of plausible impact scenarios; (2) MRI data, processed to obtain detailed brain geometry for FE model personalization and to identify observed injury locations; and (3) a detailed finite element model of the human head (THUMS v4.02), personalized using the patient's MRI. The pipeline involves subjecting the personalized head model to a large number of impact scenarios generated using a Monte Carlo-based design of experiments (DOE), constrained by the available accident information. For each simulation, injury patterns (in the skull and brain) are predicted based on stress and strain metrics. The predicted injury locations are then compared with those observed in the patient. A surrogate-based optimization is subsequently used to further explore the best-performing region of the parameter space and identify additional candidate impact configurations.

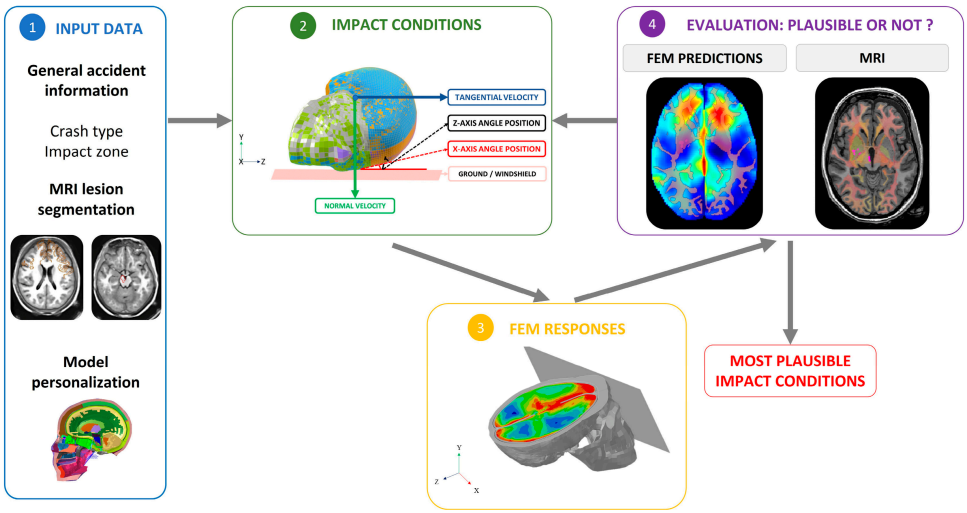

Figure 1. Schematic overview of the method used to analyze imaging data and finite element model responses.

2.1. Studied Clinical Case

This case study is based on a participant enrolled in the MRI-COMA clinical trial (NCT00577954), conducted at Pitié-Salpêtrière University Hospital between 2010 and 2020. To protect patient privacy, only limited demographic information is reported. The patient was a young adult female, approximately 170–180 cm tall. The patient was struck by a motor vehicle while walking. Upon initial evaluation, she had a Glasgow Coma Scale score of 8/15, left areflexic mydriasis and left hemiplegia. An initial CT scan revealed fractures of the left malar tripod, orbital floor, and maxilla (Figure 2A), as well as the absence of a hemorrhagic

cerebral lesion. The left-sided hemiplegia suggested a lesion in the mesencephalon of the corticospinal tract. No clinical-radiological correlation was noted on the initial CT scan. A subsequent MRI detected a lesion at 22 days after the impact (Figure 2B), indicating a temporal discrepancy between the radiological findings and symptoms. Assessment of the anatomical lesions detected using a lesion segmentation pipeline [30] reveals the presence of symmetric, bilateral microbleeds predominantly located in the cortical brain, such as the orbital frontal area, temporal lobe, occipital lobe, and parietal lobe, as well as the cerebellum (Figure 2B–D, shown in red). A few microbleeds were visible in the deep brain nuclei, particularly in the lenticular nucleus of the left and right basal ganglia, the right thalamus, the corpus callosum, and the right corticospinal tract. Normalized fractional anisotropy (FA) was also analyzed (Figure 2B–D in brown). Differences in anisotropy were found in the gray matter of the frontal, parietal, and temporal lobes, as well as in the white matter diffusely (Figure 2B–D in brown).

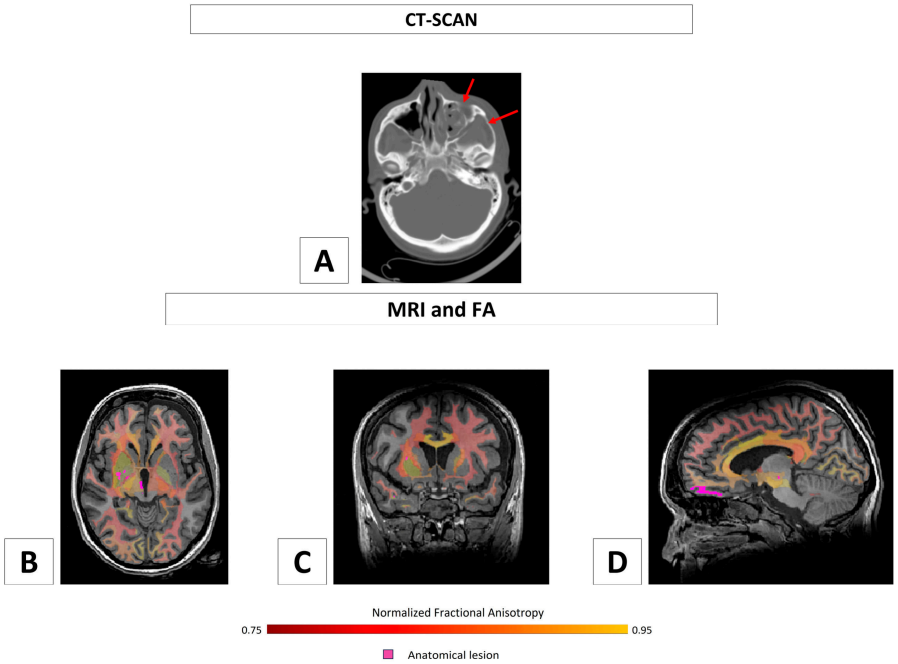

Figure 2. Lesions assessment of the initial CT scan, indicating fractures of the left malar tripod, orbital floor, and maxilla (red arrows) (**A**), the T1 MRI microbleeds (in pink) and the normalized fractional anisotropy (yellow to red) in axial (**B**), coronal (**C**), sagittal (**D**) plane 22 days after the accident.

2.2. MRI Analysis and Segmentation: Brain Structures, Conventional Lesion and Fractional Anisotropic

Patient-specific brain structures were segmented from 3D T1-weighted MRI images using the image-processing method developed by Simeone et al. [5]. This method applies an advanced MRI post-processing pipeline to segment and reconstruct patient-specific brain structures. Initially, both baseline and follow-up MRIs were processed using the Free Surfer "recon-all" pipeline with default parameters [31,32], including motion correction, skull stripping, intensity normalization, segmentation, and cortical surface reconstruction. All outputs were visually inspected to ensure anatomical accuracy. To improve measurement accuracy, the images were reprocessed using the FreeSurfer longitudinal pipeline, which generates a subject-specific template through inverse-consistent registration to estimate changes in cortical volume, thickness, and surface area [33,34]. Lesions such as hematomas, oedemas and contusions were identified [35]. Contusions were segmented using an algo-

rithm that takes intensity levels into account to identify edema and hematoma. Fractional anisotropy (FA) data were integrated using brain Quant 1.1 [5,30].

Because MRI was acquired 22 days after injury, FA abnormalities exploited in the second analysis were not considered direct measures of the instantaneous deformation occurring during impact. Instead, we hypothesized that the initial mechanical loading contributed to the spatial distribution of the tissue alterations subsequently detected by diffusion MRI, consistent with experimental studies linking brain strain and strain rate to later changes in diffusion MRI metrics [36]. FA was therefore used as an indirect marker of potentially impact-related tissue alteration, while acknowledging that secondary biological processes may also contribute to the observed abnormalities.

2.3. Head Finite Element Model Description and Personalization

This study used the Total Human Model for Safety (THUMS) v4.02, a 50th percentile male model developed by Toyota Motor Corporation and Toyota Central R&D Labs., Inc. (JP-23), in LS-DYNA software (LS-DYNA R11.1.1, LSTC, CA, USA). The head model includes the skin, individual bones of the skull, meninges (dura mater, arachnoid mater, and pia mater), and cerebrospinal fluid (Figure 3). The brain comprises the cerebrum, cerebellum, and brainstem, which are subdivided into gray and white matter. The model also includes the lateral and third ventricles of the ventricular system (Figure 3). The mechanical behavior of brain tissue was represented using a homogenous linear viscoelastic Maxwell-Kelvin model [37]. The model was validated for brain deformation and pressure using Nahum et al. (1977) [18] and Hardy et al. (2001) [19]. The THUMS head model was selected due to its high anatomical fidelity, extensive validation, and widespread adoption within the scientific community for automotive, sports, and clinical applications [38,39]. THUMS v4.02 was selected because it was the version available when the study was initiated and its head/brain formulation remains largely comparable to later versions. Rather than relying on sex-specific models available in more recent THUMS versions, the model was personalized using the patient's MRI-derived brain volume and anatomy, providing a consistent framework applicable to both male and female cases.

The THUMS head model was personalized based on the method developed by Bouvette et al. [40]. Briefly, after segmentation from MRI data, patient-specific brain structures were further processed using the 3D Slicer platform (Figure 4A). The generic THUMS model (initial brain volume: 1,452,520 mm^3) was isotropically scaled to match the patient's brain volume (1,708,220 mm^3), using a uniform scale factor of 1.056. This method was supported by previous studies showing that subject-specific mechanical responses were similar between volume-based scaled models and fully morphed models [41,42].

Additional brain structures were incorporated into the model, including the basal ganglia, corpus callosum, corticospinal tract, thalamus, and ventricular system. To achieve this, the entire brain segmented from the MRI was first rigidly registered to the corresponding brain geometry of the scaled THUMS model using the SlicerCMF module (Figure 4B). Each segmented brain structure was then exported in STL format and imported into the FE pre-processing environment (Altair HyperWorks, Altair Engineering Inc., Detroit, MI, USA). Elements of the THUMS brain mesh located within each imported structure were assigned to the corresponding anatomical region. Grey matter properties were assigned to the thalamus and basal ganglia, cerebrospinal fluid (CSF) properties to the ventricular system, and white matter properties to the remaining structures in HyperWorks (Figure 4C,D). The comparison between the generic THUMS model and the partially personalized head model is presented in Figure 3. Mesh quality, including element size and shape, was evaluated and remained largely unchanged, as expected following uniform isotropic scaling (Appendix A, Table A1).

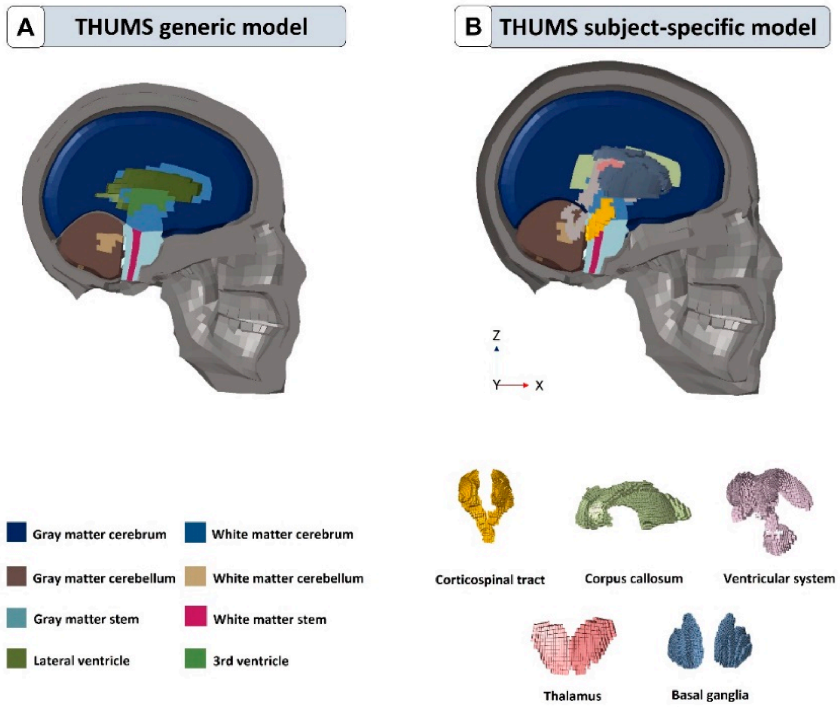

Figure 3. Comparison between the original THUMS v4.02 head model and the personalized head model. (**A**) Original THUMS model and its internal structures before scaling to the patient's brain volume. (**B**) Personalized THUMS model after scaling and incorporation of patient-specific MRI-derived anatomical regions.

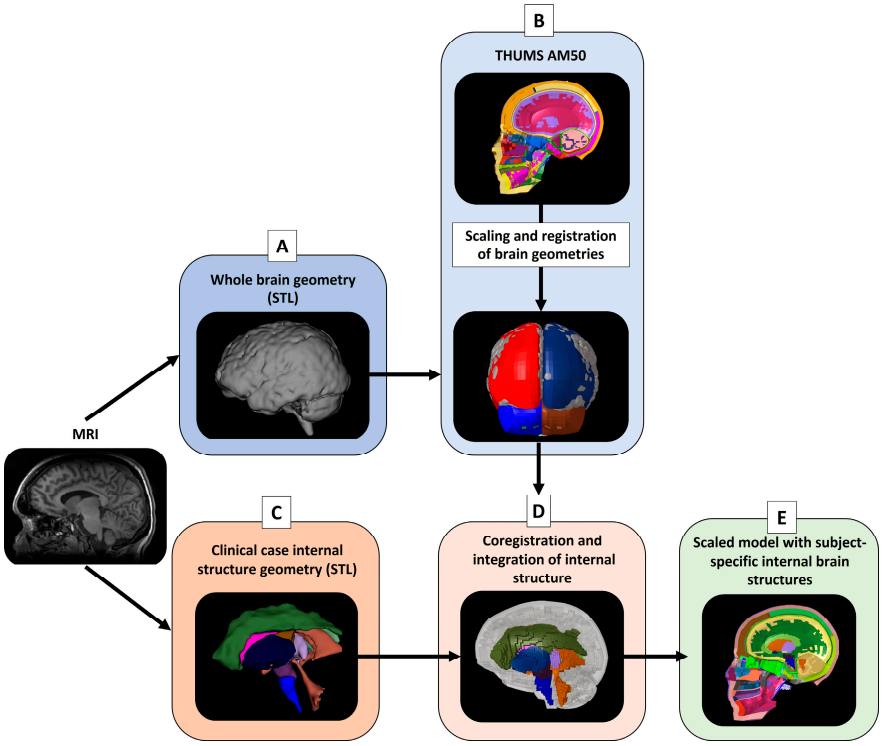

Figure 4. FE model personalization workflow. (**A**) Whole-brain geometry reconstructed from MRI (STL format). (**B**) THUMS AM50 reference model used for brain geometry scaling and registration. (**C**) Patient-specific internal brain structure geometries reconstructed from MRI (STL format). (**D**) Co-registration and integration of patient-specific internal brain structures. (**E**) Personalized FE model incorporating subject-specific brain geometries and internal structures.

2.4. Design of Experiments for Simulated Head Impacts

2.4.1. Definition of DOE Boundaries

Five impact parameters were investigated in the simulated head impacts (Figure 5): the impact location -defined by two independent head-to-ground angles along the X and Z axes, the normal and tangential impact velocities along the Y and Z axes, and the head impact surface (ground or windshield). Head impact velocities were defined based on car–pedestrian accident reconstruction studies, which reported normal impact velocities ranging from 3 to 7 m/s with a median of 5.1 m/s, (interquartile range [IQR]: 3.9–6.1 m/s) and tangential impact velocities ranging from 0 to 6 m/s with a median of 2.6 m/s (IQR: 1.0–4.9 m/s) [43,44].

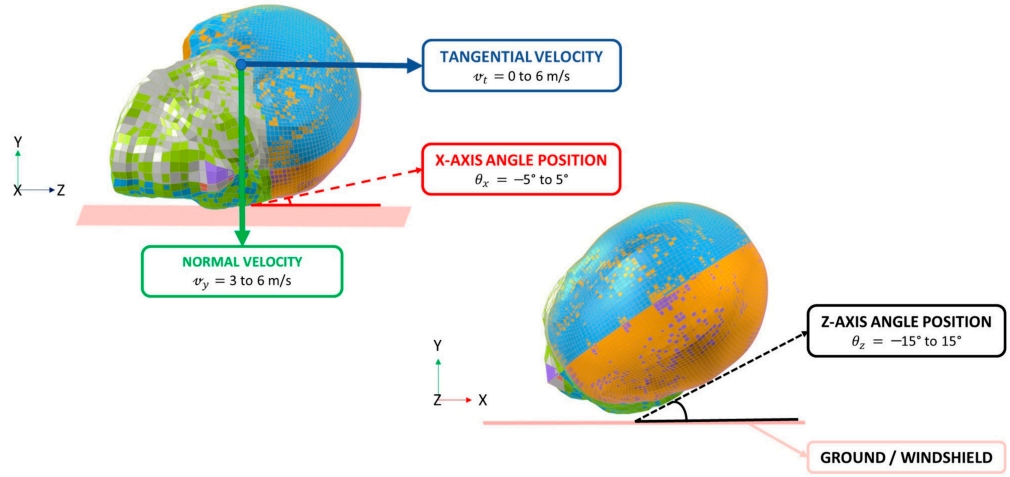

Figure 5. Impact parameters used to define the head impact conditions.

The impact location was defined based on the location of the skull fractures. Fractures of the left malar tripod, orbital floor, and maxilla were considered consistent with an impact occurring within a region extending from the lower left aspect of the left orbit to its upper central region. In the model, the impact location was defined by two positions: θ_X about the X-axis angle position (ranging from −5° to 5°) and θ_Z about the Z-axis angle position (ranging from −15° to 15°).

Two head impact surfaces were considered based on accident reconstruction data: impact with the ground [43] and impact with the vehicle windshield [44]. In the simulations, the ground was modeled as a meshed surface with linear elastic material properties (Appendix B, Figure A1) via HYPERWOKS software (Altair Engineering Inc., Detroit, MI, USA). The windshield model used in this study was extracted from a detailed finite element model of a 2010 Toyota Yaris developed by the Center for Collision Safety and Analysis (CCSA) (Appendix B, Figure A2) [45]. Mechanical properties of both surfaces are detailed in Appendix B. Contact interfaces were defined between the head model and the impact surfaces, with friction coefficients of 0.4 for the ground and 0.02 for the windshield, consistent with values reported in the literature.

To explore a range of plausible impact conditions, 120 simulations were performed using a Monte Carlo-based design of experiments, in which values for the normal and tangential impact velocities and impact orientation (X- and Z-axis angles) were randomly sampled from the predefined ranges, while the impact surface was varied between the ground and windshield. Simulation quality was assessed across all 120 simulations, with added mass remaining below 10% in all cases (mean: 3.6%).

2.4.2. Finite Element Responses Analysis and Best Impact Scenario Selection

In order to identify plausible impact scenarios explaining the observed lesion, the predicted injury locations are then compared with those observed in the patient MRI. The lesion areas identified on T1-weighted MRI and/or the regions exhibiting abnormal fractional anisotropy (FA) were segmented, exported in STL format, and imported into the finite element (FE) model while ensuring accurate spatial registration. The elements of the THUMS brain mesh lying within the imported lesion volumes were identified and classified as the injured group, whereas all other elements were classified as the non-injured group.

Two analyses were performed:

- First analysis (T1-weighted MRI only): the injured group consisted of 1579 elements (1.30% of brain elements) located within lesion areas identified on T1-weighted MRI (microbleeds), while the non-injured group consisted of 119 528 elements (98.70%).
- Second analysis (T1-weighted MRI + FA): the injured group consisted of 52 996 elements (43.76% of brain elements) identified within regions showing either lesions on T1-weighted MRI or abnormal fractional anisotropy (FA), while the non-injured group consisted of 68 111 elements (56.24% of brain elements).

Brain injury prediction in the FE model was conducted using Maximum Principal Strain (MPS) with an injury threshold value set at 0.20, based on the work reported in Zhang et al. (2024) in which the THUMS model was used [22]. The same threshold was used for both cerebral microbleeds and FA abnormalities. For both the injured and non-injured element groups, the percentage of elements exceeding the threshold was calculated relative to the total number of elements in each group. The element-based approach is equivalent to a volumetric approach.

To evaluate the predictive performance of each simulation, we computed in the brain the rates of true positives (TP), false positives (FP), false negatives (FN), and true negatives (TN) [46–48]. True positives were defined as elements correctly predicting a lesion within the injured group; false positives as elements incorrectly predicting a lesion within the non-injured group; false negatives as elements failing to predict a lesion within the injured group; and true negatives as elements correctly predicting the absence of a lesion within the non-injured group [47,48].

To take into account all four classes of the confusion matrix and the imbalanced classes the Matthews correlation coefficient (MCC) was calculated [49,50]:

$$\mathrm{MCC} = \frac{\mathrm{TP} \times \mathrm{TN} - \mathrm{FP} \times \mathrm{FN}}{\sqrt{(\mathrm{TP} + \mathrm{FP}) \cdot (\mathrm{TP} + \mathrm{FN}) \cdot (\mathrm{TN} + \mathrm{FP}) \cdot (\mathrm{TN} + \mathrm{FN})}}$$

We also calculated the F1 score, a commonly used metric that balances precision and sensitivity:

$$\text{F1 score} = 2 \times \frac{\text{Precision} \times \text{Sensitivity}}{\text{Precision} + \text{Sensitivity}}$$

where precision is defined as the proportion of elements correctly predicting injury among all elements predicting injury:

$$\text{Precision} = \frac{\mathrm{TP}}{\mathrm{TP} + \mathrm{FP}}$$

and sensitivity as the proportion of elements correctly predicting injury within the actual injured region:

$$\text{Sensitivity} = \frac{\mathrm{TP}}{\mathrm{FN} + \mathrm{TP}}$$

We also analyzed the proportion of non-lesion structures via the true negative rate (specificity):

$$\text{Specificity} = \frac{\mathrm{TN}}{\mathrm{FP} + \mathrm{TN}}$$

The MCC-F1 curve was created to determine the best reproduction of the observed injury pattern in the clinical case [51]. The MCC-F1 curve is used to evaluate binary classifiers, with the F1 score plotted on the x-axis and the MCC on the y-axis. The highest point on this curve is represented by the best trade-off between the MCC and the F1 score, allowing the simulation with the best performance to be identified [51]. A sensitivity analysis was conducted using generalized linear models (GLMs) to identify the parameters and interactions influencing the sensitivity, the precision, the F1 score, the specificity and the MCC. The models' specifications included the main effects of the type of impact (ground or windshield), the normal and tangential velocity, the X and Z axes position angles, as well as their interactions. The predictor effects were evaluated through coefficient statistics, which include the estimate, standard error, z-value, and the corresponding *p*-value and β coefficient. Data results are available in Appendix D. Analyses were performed using Python 3.9 version.

Finally, for the visualization of stress and strain patterns from the best simulation (Figure 6), a pipeline was developed to convert FE simulation results into NIfTI imaging data that can be superimposed onto the patient's MRI, enabling integration of biomechanical findings into clinical workflows and comparison using standard image analysis tools. This pipeline is described in Appendix E.

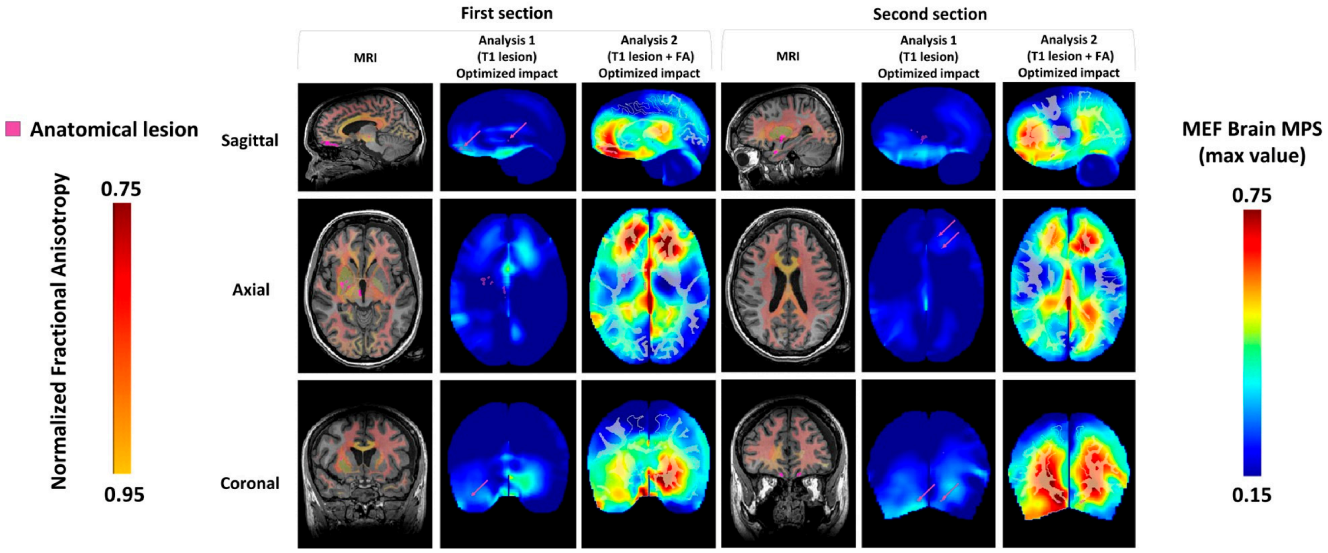

Figure 6. Comparison between numerical simulation results and patient imaging. Overlay of the simulated injury distribution with lesions identified on conventional MRI (pink arrows) and FA abnormalities (heat map) for the impact configurations identified through surrogate-based optimization in Analysis 1 (column 2) and Analysis 2 (column 3).

To further explore the impact parameter space beyond the initial 120 simulations, a surrogate-based optimization procedure approach was developed. We trained an Extra Trees regression model on the initial DOE results and performed a random search. The model was trained to predict the Matthews correlation coefficient (MCC) from the five impact parameters: impact surface, normal and tangential velocities, and head orientation angles about the X and Z axes. The dataset was divided into training (75%) and validation (25%) subsets, and the regression model was constructed using 400 trees. Its predictive performance was assessed using the coefficient of determination (R^2) and root mean square error (RMSE). This model was used to generate 10,000 random points within the parameter space, predict the MCC for each, and select the configuration with the highest predicted MCC. An additional LS-DYNA simulation was performed using the optimized parameters

to verify the surrogate model prediction and compare its performance with the prediction and the best scenario from the initial DOE. Numerical quality metrics for the configurations selected through surrogate-based optimization are presented in Appendix C.

3. Results

A total of 120 head impact simulations were performed on both solid ground and windshields, and the predicted brain injuries were compared with lesion areas identified in medical imaging (Table 1, Figures 6 and 7).

Table 1. Performance metrics by impact type for each analysis.

Analysis		Analysis 1					Analysis 2				
Impact Type	**Metrics**	**Sensitivity**	**Specificity**	**Precision**	**F1 Score**	**MCC**	**Sensitivity**	**Specificity**	**Precision**	**F1 Score**	**MCC**
Head-on-windshield	Min	0.023	0.43	0.017	0.022	0.008	0.015	0.55	0.41	0.03	−0.009
	Q1	0.20	0.66	0.022	0.041	0.048	0.082	0.74	0.55	0.14	0.069
	Median	0.41	0.85	0.029	0.052	0.060	0.21	0.88	0.57	0.31	0.137
	Q3	0.60	0.93	0.036	0.060	0.075	0.46	0.94	0.60	0.51	0.20
	Max	0.82	0.99	0.042	0.076	0.10	0.72	0.99	0.63	0.63	0.28
Head-on-ground	Min	0.072	0.09	0.014	0.028	0.025	0.033	0.13	0.44	0.062	0
	Q1	0.62	0.19	0.016	0.031	0.044	0.48	0.28	0.50	0.52	0.18
	Median	0.85	0.34	0.017	0.033	0.052	0.83	0.47	0.53	0.63	0.23
	Q3	0.98	0.63	0.022	0.041	0.065	0.92	0.71	0.55	0.66	0.30
	Max	1.00	0.97	0.045	0.081	0.11	0.98	0.97	0.60	0.68	0.34

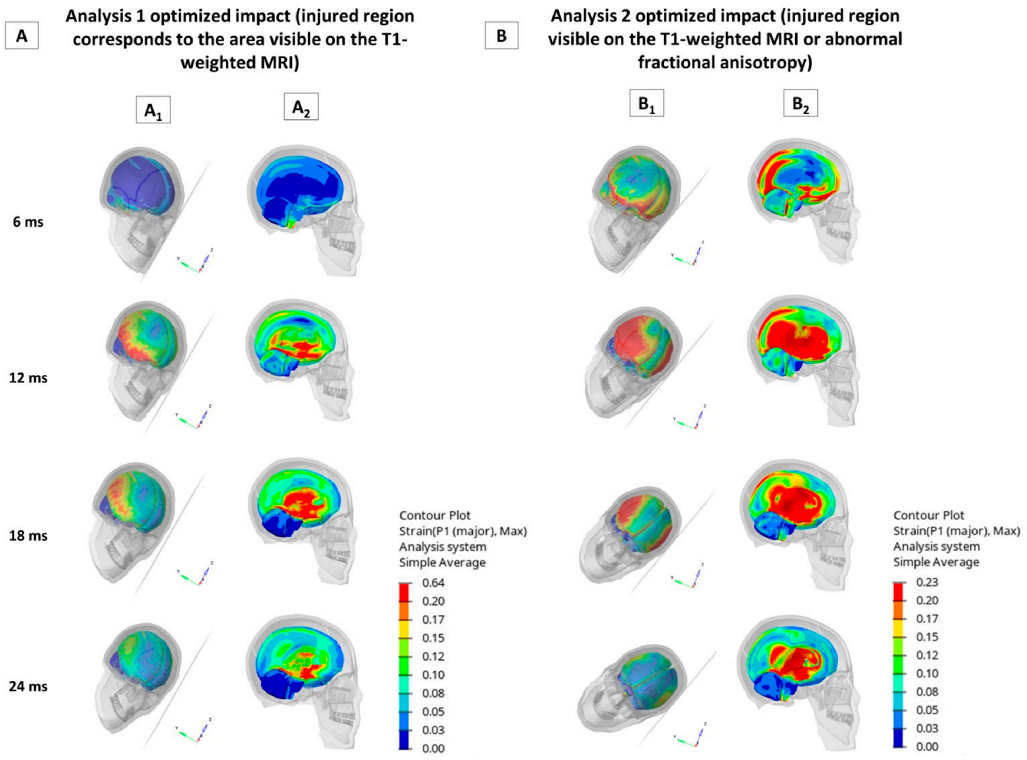

Figure 7. Distribution of maximum principal strain for the impact configurations identified through surrogate-based optimization in Analysis 1 (**A**) and Analysis 2 (**B**). Results are shown at four time points, with external views (**A1**,**B1**) and cross-sectional views of the brain (**A2**,**B2**).

3.1. Analysis 1: Injured Region Corresponds to the Area Visible on the T1-Weighted MRI

In Analysis 1, the injured regions corresponded to microbleeds in the cerebral cortex and deep brain nuclei. The model showed low performance in reproducing these injuries, meaning the predicted injured regions showed little agreement with those observed. This

limited agreement can be partly explained by the highly imbalanced classification matrix. Since injured elements represented only 1.3% of the brain, accurately localizing lesions within such restricted regions was particularly challenging. This low performance was confirmed by MCC values ranging from 0.008 to 0.11 (Table 1). Even after surrogate-based optimization, the selected configuration achieved an MCC of only 0.11 and an F1 score of 0.07, with high specificity (0.84) but low sensitivity (0.51) (Figure 8). This simulation corresponded to a head-to-ground impact with normal and tangential velocities of 3.21 and 1.01 m/s, respectively, and head orientation angles of −0.94° about the X-axis and −0.73° about the Z-axis (Figures 7 and 8). The maximum von Mises stress in the left malar tripod reached 130 MPa, exceeding stress levels previously associated with facial-bone fracture initiation (approximately 80–100 MPa) [52], consistent with the observed facial fracture.

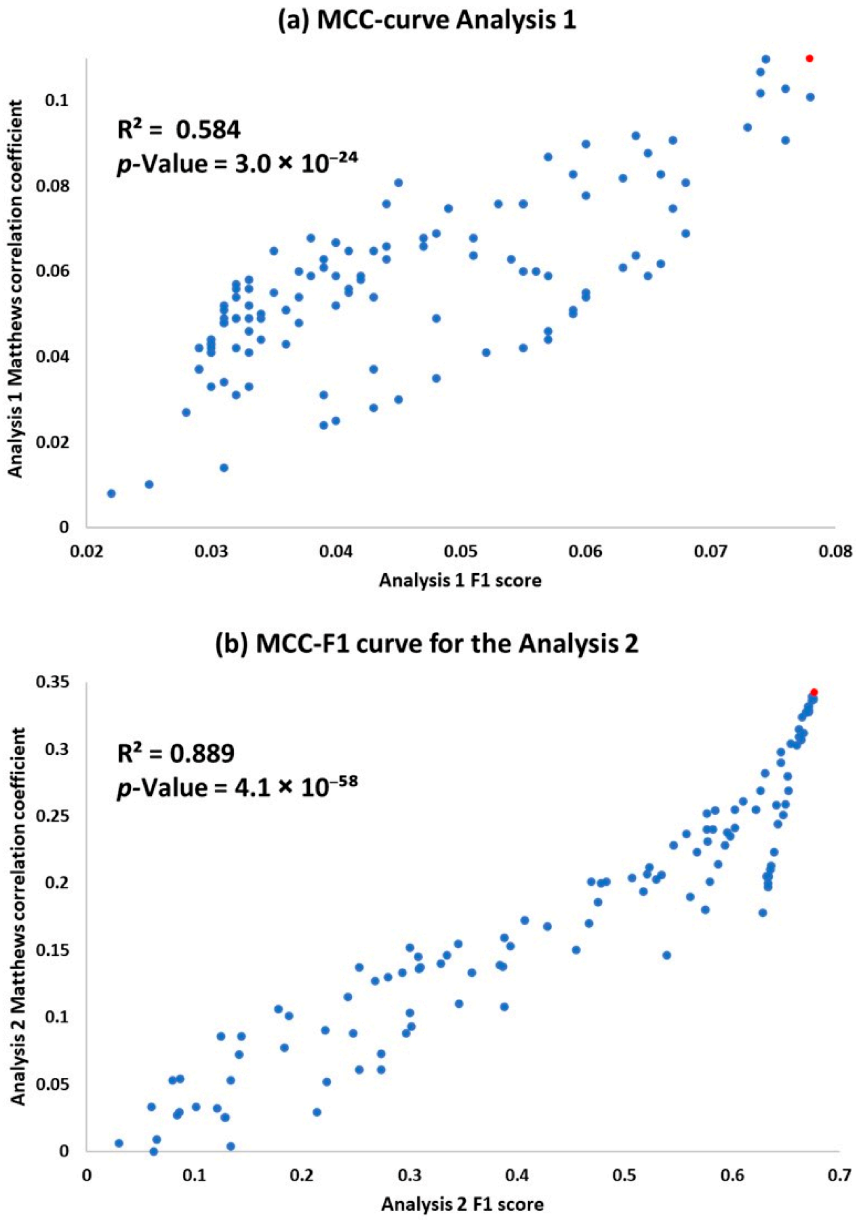

Figure 8. F1 score vs. Matthews coefficient correlation for the Analysis 1 (injured region corresponds to the area visible on the T1-weighted MRI) and Analysis 2 (injured region on the T1 weighted MRI or abnormal fractional anisotropy). The impact configurations identified through surrogate-based optimization for each analysis are highlighted in red.

3.2. Analysis 2: Injured Region Corresponds to the Area Visible on the T1-Weighted MRI or Abnormal Fractional Anisotropy

When the injured region was defined as areas showing either lesions on T1-weighted MRI or abnormal fractional anisotropy (analysis 2), these injured regions represented 43.76% of the brain elements and the model performance improved due to a better localization and volume of lesion areas, with F1 scores ranging from 0.03 to 0.68 and MCC values ranging from 0.006 to 0.34 (Figure 7, Table 1). Impact type and normal impact velocity were the two most influential factors affecting the MCC. Windshield impacts were associated with a lower MCC compared with ground impacts ($\beta = -0.092$, 95% CI: $[-0.11, -0.075]$), mainly due to a decrease in sensitivity ($\beta = -0.42$), although this was accompanied by increases in precision ($\beta = 0.038$) and specificity ($\beta = 0.339$). Similarly, higher impact velocities were associated with increased MCC ($\beta = 0.038$, 95% CI: $[0.026, 0.050]$), driven by improved sensitivity ($\beta = 0.13$), but also accompanied by improvement in precision ($\beta = 0.0019$) but a decrease in specificity ($\beta = -0.097$). The X angle, as well as the interaction between the X and Z angles, significantly affected the F1 score, with smaller X angles that is, a lower maxillary impact, closer to the mandible than to the orbit being associated with higher MCC values.

Among the fifteen best-performing simulations, characterized by F1 scores greater than 0.66 and MCC values greater than 0.31, normal impact velocities ranged from 4.79 to 7.00 m/s, while Z-axis impact angles ranged from −15° to 2.19°. These impacts were located on the lower part of the maxilla that is, closer to the orbit than to the mandible and on its posterior part, closer to the zygomatic bone than to the nose. Following surrogate-based optimization, the selected configuration for Analysis 2 achieved an MCC of 0.34 and an F1 score of 0.68. This simulation corresponded to a head-to-ground impact with normal and tangential velocities of 5.41 and 3.21 m/s, respectively, and head orientation angles of 1.82° about the X-axis and −9.94° about the Z-axis (Figure 6, Table 1). It exhibited high sensitivity (0.90) but relatively low specificity (0.41), indicating overestimation of the injured brain regions (Figures 7 and 8). The maximum von Mises stress in the left malar tripod reached 237 MPa, exceeding stress levels previously associated with facial-bone fracture initiation (approximately 80–100 MPa) [52], consistent with the observed facial fracture.

4. Discussion

This study provides proof of concept for a reverse-engineering framework aimed at identifying plausible head impact conditions from post-traumatic brain imaging. In contrast to conventional forward approaches, which estimate tissue response from known or assumed loading conditions, the present method starts from observed lesions and seeks the impact scenarios that are most consistent with them. The methodology was applied to a case study involving a subject who sustained a severe brain injury associated with a malar floor fracture. Microbleeds identified on T1-weighted MRI and regions of abnormal fractional anisotropy measured using diffusion tensor imaging (DTI) were used as imaging markers of injury. A partially personalized finite element brain model was subjected to impacts consistent with the malar floor fracture under varying impact velocities, angles, and contact surfaces. Regions of high brain strain predicted by the FE simulations were compared with the observed lesion locations. In the first analysis, based on only on T1-weighted MRI findings, the best-fit scenario achieved an overall low MCC (0.11) with a high specificity (0.849) but a low sensitivity (0.50), indicating the difficulty of capturing the highly localized and dispersed nature of the T1 lesions, with the spatial resolution of the present inverse modeling framework. However, when both microbleeds and regions of abnormal fractional anisotropy were included in the analysis, the model demonstrated

substantially improved predictive capability (MCC = 0.34 with sensitivity =0.884). It was also able to identify plausible impact scenarios, characterized by an impact zone located in the lower and posterior part of the maxilla, close to the mandible and zygomatic bone, and impact velocities ranging from 4 to 7 m/s. These findings provide preliminary guidelines for lesion-informed inverse reconstruction of plausible head impacts for forensic applications. They also raise questions regarding the use of post-impact fractional anisotropy alterations as a biomarker of brain deformation during impact.

A key finding of this study is that the inverse framework was able to identify a set of impact parameters associated with the observed lesion distribution. Impact type, normal velocity, and impact position along the X-axis were the most influential variables, with additional contributions from interactions between velocity and spatial coordinates. These results suggest that both loading intensity and impact location play a central role in shaping lesion distribution. These observations are consistent with previous biomechanical studies showing that the distribution of intracranial strains and the resulting injury patterns are directly influenced by the loading intensity and direction, as well as the impact location. Finite element investigations have demonstrated that rotational kinematics and impact orientation substantially affect white matter deformation and the spatial distribution of traumatic axonal injury [36,53]. Studies combining finite element simulations with neuroimaging have also reported correlations between predicted strain metrics and diffusion-based abnormalities following traumatic brain injury, supporting the relevance of diffusion-informed biomechanical approaches for injury prediction [23,36]. The present findings therefore support the growing body of evidence suggesting that subject-specific finite element approaches combined with imaging biomarkers may provide clinically and forensically meaningful information regarding traumatic brain injury mechanisms.

More specifically, plausible impact conditions were identified, including impacts near the orbit with impact velocities higher than 3.10 m/s for ground impacts and higher than 3.21 m/s for windshield impacts. This first result is particularly relevant in a forensic context, as it may help evaluate crash hypotheses and clarify injury attribution [11,54]. The objective of the study was to go further and identify plausible impact scenarios. To this end, dedicated performance metrics were developed, leading to the identification of a best-fit scenario (Figure 1). A major strength of these performance metrics is that they rely on a quantitative assessment of the correspondence between the predicted injured regions and the actual injury distribution, enabled by the personalization of the brain model and the coregistration of the finite element model with the medical imaging data, allowing the injury regions identified on MRI to be imported into the FEM post-processing environment. The surrogate-based optimization extended the exploration of impact conditions beyond the initial Monte Carlo DOE. For both imaging-based analyses, the optimized configurations yielded MCC values comparable to those of the best initial DOE simulations (0.11 for Analysis 1 and 0.34 for Analysis 2), despite differences in impact parameters, particularly tangential velocity. These findings indicate that different combinations of impact parameters can achieve similar performance metrics, without necessarily producing identical strain distributions. This highlights the potential non-uniqueness of the inverse reconstruction. Accordingly, the identified configurations should be interpreted as plausible impact scenarios rather than uniquely determined impact conditions. When considering only the microbleed lesions visible on T1-weighted MRI sequences, the best simulation showed good specificity (0.849) by correctly predicting non-lesion areas. However, it also showed limited sensitivity (0.50), meaning that it missed a substantial proportion of injury locations. A possible explanation for this low sensitivity is that the dispersed and microscopic nature of the T1 lesions in this specific case may exceed the spatial resolution and localization accuracy achievable with the present finite element brain model. We

therefore expect the predictive capability of the model to improve in cases involving larger and less spatially dispersed areas of brain injury, as previously demonstrated in several computational studies [23,36].

The comparison between conventional MRI and FA-based lesion analysis was particularly informative. The model showed substantially better agreement with diffuse FA disruptions than with the highly localized lesions identified on conventional T1-weighted MRI (sensitivity: 0.884). However, this apparent improvement should be interpreted cautiously. The proportion of brain elements classified as injured increased substantially from 1.30% in Analysis 1 to 43.76% in Analysis 2, substantially changing the classification problem and likely contributing to the higher MCC values observed in Analysis 2. Moreover, even the best-performing simulation achieved only a moderate MCC of 0.34 and a low specificity of 0.43, indicating substantial overprediction of injured regions. Beyond this classification effect, the difference between the two analyses may also reflect the spatial characteristics of the imaging abnormalities. The T1 lesions were highly localized and dispersed, making them more difficult to reproduce at the spatial resolution of the present inverse modeling framework. In contrast, the more diffuse FA alterations may better reflect the overall distribution of brain deformation during impact and therefore show greater spatial agreement with the strain-based metrics derived from the finite element model (Figure 7). This difference may also be related to the distinct pathophysiological processes represented by the two imaging markers. Microbleeds identified on T1-weighted MRI primarily reflect vascular injury, including damage to small cerebral vessels, whereas FA abnormalities are more closely associated with alterations in white matter microstructure and axonal organization [55–57]. Consequently, FA abnormalities may be more directly related to the mechanical deformation of brain tissue and therefore more closely associated with the strain-based injury metric used in the finite element model. In contrast, the occurrence of microbleeds may depend not only on tissue deformation but also on vascular-specific factors that are not explicitly represented in the present model [58]. Importantly, however, the same deformation threshold was used to define simulated injury regions for comparison with both T1-weighted microbleeds and FA abnormalities. This represents an important methodological simplification that may affect the ranking of the reconstructed scenarios, as vascular and axonal injuries may have different mechanical tolerances and may therefore require distinct injury criteria or thresholds [55,56]. To assess the influence of this choice, a sensitivity analysis was conducted using alternative MPS thresholds reported in the literature (Appendix F). The scenario ranking remained largely consistent, with strong correlations in MCC values ($R^2 = 0.97$ for 0.21, $R^2 = 0.90$ for 0.18 and $R^2 = 0.79$ for 0.26 compared with the 0.20 threshold) and substantial overlap among the best-performing simulations. Future work should investigate imaging-specific injury thresholds, or complementary mechanical metrics, to better account for these different underlying injury mechanisms.

An important aspect of this study is the integration of FA as a lesion-related imaging marker. Although FA should not be interpreted as a direct measure of mechanical deformation, it provides a biologically meaningful surrogate of white matter microstructural organization and disruption [59,60]. This interpretation is supported by numerous studies demonstrating that alterations in FA reflect structural damage following traumatic brain injury [5]. Beyond its role as an imaging biomarker, FA has also been used to inform computational brain models. In particular, diffusion-derived information has been related to the mechanical anisotropy of white matter in finite element models [61,62], while FA has been incorporated into finite element and micromechanical approaches to represent white matter heterogeneity, refine mesh or material descriptions, and improve the prediction of axonal deformation and injury risk [63–65]. Furthermore, several studies have reported

associations between FE-predicted deformation metrics and post-traumatic diffusion abnormalities, supporting the relevance of diffusion-informed biomechanical modeling for white matter injury prediction [36,59,66]. The better agreement obtained with FA-based analysis in the present study therefore strengthens the rationale for combining structural MRI with diffusion-derived information in reverse biomechanics. More broadly, these findings are consistent with the known limitations of conventional MRI in traumatic brain injury: although it remains the clinical standard for detecting macroscopic lesions, it has limited sensitivity for diffuse or microscopic white matter damage. In contrast, diffusion-derived measures provide information on white matter organization and may better capture the directional vulnerability of axonal pathways and the diffuse nature of traumatic axonal injury [5,67].

The proposed reverse-biomechanics approach offers promising perspectives because it relies on post-traumatic CT and MRI data that are commonly acquired in clinical practice. Its most immediate application is likely to be in detailed forensic or research case studies, where the time required for subject-specific reconstruction and analysis is compatible with the investigation process [11,68]. The framework may also support retrospective clinical studies aimed at improving the understanding of injury mechanisms and their relationship with observed imaging findings [23,69]. With further methodological development, increased automation, and validation across larger patient cohorts and a broader range of injury and impact conditions, the approach could ultimately provide useful complementary information for clinical assessment. At present, however, such clinical applications remain exploratory.

Limitations

The present study proposes a methodology for predicting impact conditions from post-traumatic imaging data and provides a proof of concept through its application to a single case study. Further validation in a larger cohort will be required to assess its robustness and generalizability. Applying the proposed methodology to a larger number of cases will enable progressive refinement of the framework, extend its applicability across a broader range of injury mechanisms and lesion patterns, and ultimately establish a generalized methodology capable of identifying the best-fit impact scenario for a wide variety of traumatic brain injuries.

Another important set of limitations relates to the finite element brain model itself. First, the model was only partially patient-specific. Although the THUMS head was scaled to the patient's brain volume and MRI-derived brain regions were incorporated, the skull and facial geometry remained generic. This may affect local contact conditions, facial stress distributions, and load transmission to the brain. Future work should incorporate patient-specific craniofacial geometry and recent advances in facial FE modeling, including refined anatomy, validation, and fracture criteria [70], to improve the identification of plausible impact locations and directions and provide more reliable estimates of the loads transmitted from the face to the brain.

The DOE did not include initial head angular velocity, although rotational velocity and acceleration generated by the impact were captured by the FE model. Because representative pre-impact angular velocities are not well documented for this type of crash scenario, this parameter was not varied, but should be considered in future reconstructions. In addition, the model did not include the neck or whole-body dynamics. This may affect head kinematics at impact and the mechanical coupling between the head, spinal cord, and brain, potentially influencing predicted brain strain [71,72]. Future work should therefore incorporate initial rotational velocity and coupled head–neck dynamics.

Also, the assumption of homogeneous material properties within anatomically complex brain regions remains a simplification. Some accident victims may have had a pre-existing pathological brain condition prior to the accident, and this should be taken into account when creating a patient-specific model [15,73]. Experimental studies have demonstrated regional differences in white matter mechanical behavior that may influence brain deformation during impact [15,73], and brain tissue mechanical properties are also known to vary substantially between individuals. In addition, the present study relied on published injury thresholds derived from the THUMS brain model to define injured regions. However, the use of binary injury thresholds has been widely debated in the literature, as such approaches may not fully capture the complex and multifactorial pathophysiology of traumatic brain injury [22], nor the known inter-individual variability in tolerance to head impacts [21,41]. We attempted to mitigate some of these limitations through partial geometric personalization and by using a brain model with experimentally validated kinematic responses. Nevertheless, future developments linking MRI-derived information to brain biomechanics may provide opportunities to further personalize tissue mechanical properties and improve model predictions [41].

5. Conclusions

This study proposed a reverse-engineering framework to identify plausible head impact conditions from patient-specific post-traumatic imaging data. The approach combines personalized finite element head modeling, a Monte Carlo-based design of experiments, and quantitative comparison between simulated brain strain patterns and lesions observed on conventional MRI and fractional anisotropy maps. By systematically varying five impact parameters—impact surface, normal and tangential velocities, and impact orientation along the X- and Z-axes—the method aimed to identify plausible impact scenarios that best reproduced the observed injury pattern. The approach was unable to reproduce the microbleeds scattered throughout the brain accurately. However, plausible impact scenarios were obtained when the lesions were more extensive, particularly when fractional anisotropy (FA) abnormalities were also considered. The results support the potential of finite-element-based biomechanical reconstruction to improve the understanding of traumatic brain injury mechanisms. In particular, the integration of diffusion-derived information improved the agreement between simulated and observed injury patterns, suggesting that fractional anisotropy alterations may provide a relevant imaging marker of post-traumatic white matter disruption associated with brain deformation. These findings highlight the value of combining biomechanical modeling with advanced neuroimaging for personalized trauma analysis.

Author Contributions: Conceptualization, T.M., P.S., C.D. (Clémence Delteil), L.T., N.B., L.P. and É.W.; Methodology and investigation, T.M., P.S., C.D. (Clémence Delteil), V.B., C.D. (Cyrile Duquenoy), J.-L.M., Y. Godio-Raboutet, É.W., L.T. and N.B.; Supervision, P.S., C.D. (Clémence Delteil), J.-L.M., Y.G.-R., É.W., L.T. and N.B.; Writing—original draft preparation, T.M.; Writing—review and editing, T.M., P.S., C.D. (Clémence Delteil), L.T., N.B., L.P. and É.W. All authors have read and agreed to the published version of the manuscript.

Funding: This research received no external funding. The MRI-COMA trial was funded by independent research grants from non-profit or governmental agencies: the French Ministry of Health, Paris, France (Programme Hospitalier de Recherche Clinique 2005 #051061), and the French National Agency for Research (ANR) for the program "Investissements d'avenir" ANR-10-IAIHU-06 (to the Brain and Spine Institute); Fondation des "gueules cassées.".

Institutional Review Board Statement: The patient case used in this study was extracted from the MRI-COMA database: (https://clinicaltrials.gov/study/NCT00577954?cond=Mri%20coma&viewType=Card&rank=2, consulted on the 2 October 2023), which received approval from the local

ethics committee on the 10 July 2014 (Comité de Protection des Personnes, CPP XI; authorization no. 1,934,708).

Informed Consent Statement: In accordance with French law, patients and their relatives were informed of their inclusion in the MRI-COMA database, and informed consent was obtained from participants or their legal representatives before follow-up assessments.

Data Availability Statement: The data presented in this study are available on request from the corresponding author.

Acknowledgments: The authors thank Julien Sein and David Meunier for their assistance with MRI analysis and segmentation. This work was developed with the assistance of AI tools. Specifically, ChatGPT version 4 and 5.0 was used to generate elements of statistical code in Python (Version 3.9, Python Software Foundation, Wilmington, DE, USA), as well as to aid in the synthesis of content and refinement of vocabulary. However, all AI-generated content was reviewed, adapted, and verified by the author to ensure accuracy, relevance, and alignment with the study's objectives.

Conflicts of Interest: The authors declare no conflicts of interest.

Abbreviations

The following abbreviations are used in this manuscript:

CT	Computed tomography
CSF	Cerebrospinal fluid
CCSA	Center for Collision Safety and Analysis
DOE	Design of experiments
DTI	Diffusion tensor imaging
FA	Fractional anisotropy
FE	Finite element
FEM	Finite element model
GLM	Generalized linear model
IQR	Interquartile range
MCC	Matthews correlation coefficient
MPS	Maximum Principal Strain
MRI	Magnetic resonance imaging
NIfTI	Neuroimaging Informatics Technology Initiative
TBI	Traumatic brain injury
THUMS	Total Human Model for Safety

Appendix A

The evaluation of the generic and the partially personalized THUMS model included element size, Jacobian quality, aspect ratio, and the number of elements failing the predefined quality criteria. The results of this comparison are presented in Table A1.

Table A1. Comparison of mesh quality metrics between the original THUMS v4.02 head model and the personalized head model.

Mesh Quality Metric		Original THUMS v4.02		Personalized THUMS	
		2D Elements	3D Elements	2D Elements	3D Elements
Minimum element size (mm)		0.11	0.13	0.119	0.14
Minimum Jacobian determinant		0.29	0.25	0.29	0.25
Warpage		76.73	78.56	76.73	78.56
Maximum aspect ratio		23.90	17.18	23.90	17.18
Minimal angles	**Tria**	2.63	3.01	2.63	3.02
	Quad	8.99	11.34	8.99	11.34
Maximal angles	**Tria**	170.93	168.04	170.93	168.04
	Quad	174.15	175.52	174.15	175.52

Appendix B

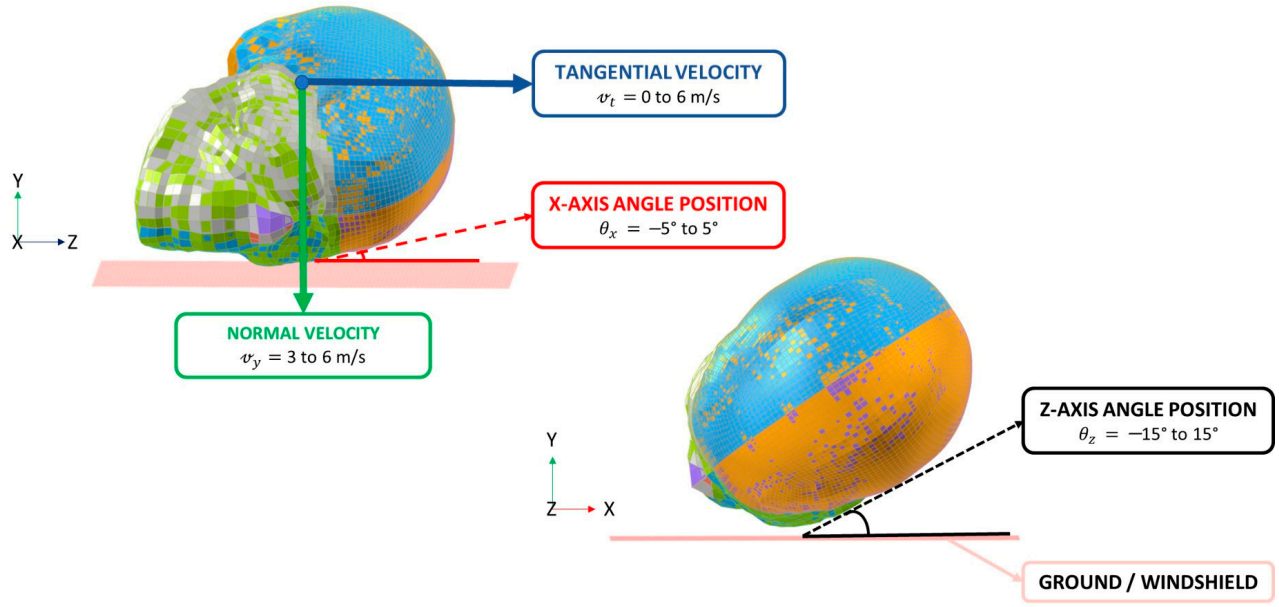

Structures	Material	Density (g/cm^3)	Module Young (MPa)	Poisson's ratio
Ground	Linear Elastic	7	200,000	0.4

Figure A1. Material properties and impact conditions on the ground.

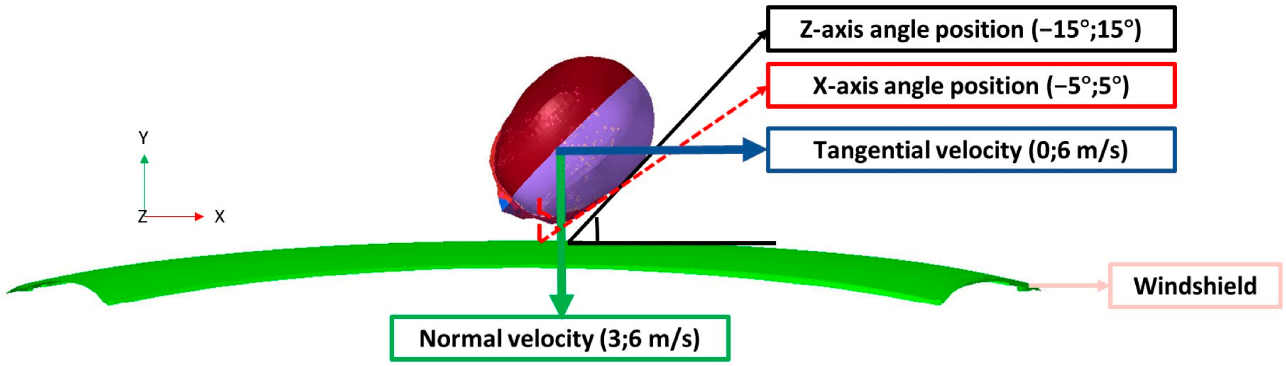

Structures	Windshield top	Windshield midlayer	Windshield back
Material	Elastic-Plastic		
Density	2.5	1	2.5
Young modulus (MPa)	70,000	250	70,000
Poisson's ratio	0.22	0.35	0.22
Yield stress (pressure) (MPa)	30	10	30
Tangent modulus (MPa)	1,000	1	1,000
Failure Flag	0.015	2.5	0.015

Figure A2. Material properties and impact conditions on the windshield of the 2010 Toyota Yaris De-tailed Finite Element Model.

Appendix C

Table A2. Numerical quality metrics for the simulation of the configurations selected through surrogate-based optimization.

Numerical Quality Metric	Value
Added mass due to mass scaling (%)	1.7×10^{-6}
Maximum hourglass energy/reference energy (%)	13.8
Energy balance error (%)	0.5

Appendix D

Appendix D.1. Influence Parameters and Their Interactions for the Analysis 1

Table A3. Influence of the parameters and their interactions on the F1 score and the Matthews correlation coefficient for Analysis 1. Only parameters and interactions with a significant effect ($p < 0.05$) are reported.

	Parameters	*p*-Value	Standard Error	Lower 95% Confidence Interval Bound	β Coefficient	Upper 95% Confidence Interval Bound
F1 score	Type of impact *	1.46×10^{-8}	0.0020	0.0075	0.011	0.015
	Normal Velocity	0.00028	0.0015	−0.0086	−0.0056	−0.0026
	X-axis	0.037	0.0016	−0.0063	−0.0033	−0.00020
	Normal Velocity × X-axis	0.026	0.00025	6.63×10^{-5}	0.00055	0.0010
	X-axis × Z-axis	0.015	3.51×10^{-5}	1.63×10^{-5}	8.50×10^{-5}	0.00015
Matthews correlation coefficient	X-axis	0.0028	0.0025	−0.012	−0.0074	−0.0026
	Normal Velocity × X-axis	0.0091	0.00041	0.00026	0.0011	0.0019
	X-axis × Z-axis	0.0016	5.66×10^{-5}	6.81×10^{-5}	0.00018	0.00029

* Windshield: positive value and ground: negative value.

Appendix D.2. Influence Parameters and Their Interactions for the Analysis 2

Table A4. Influence of the parameters and their interactions on the F1 score and the Matthews correlation coefficient for Analysis 2. Only parameters and interactions with a significant effect ($p < 0.05$) are reported.

	Parameters	*p*-Value	Standard Error	Lower 95% Confidence Interval Bound	β Coefficient	Upper 95% Confidence Interval Bound
F1 score	Type of impact *	9.30×10^{-52}	0.016	−0.27	−0.24	−0.20
	Normal Velocity	1.58×10^{-13}	0.010	0.056	0.077	0.097
	Z-axis	0.00029	0.0039	−0.022	−0.014	−0.0065
	X-axis	0.0040	0.0093	−0.045	−0.027	−0.0085
	Normal Velocity × Z-axis	5.92×10^{-5}	0.00072	0.0015	0.0029	0.0043
	X-axis × Z-axis	0.014	0.00026	−0.0012	−0.00065	−0.00013
Matthews correlation coefficient	Type of impact *	3.21×10^{-27}	0.0085	−0.11	−0.092	−0.075
	Normal Velocity	1.11×10^{-9}	0.0062	0.026	0.038	0.050
	Z-axis	5.03×10^{-5}	0.0019	−0.012	−0.0078	−0.0041
	Normal Velocity × Z-axis	0.0013	0.00037	0.00046	0.0012	0.0019

* Windshield: positive value and ground: negative value.

Table A5. Influences of the significative parameters and their interactions on the sensitivity, the specificity and the precision for the Analysis 2.

	Parameters	*p*-Value	Standard Error	Lower 95% Confidence Interval Bound	β Coefficient	Upper 95% Confidence Interval Bound
Sensitivity	**Type of impact ***	2.19×10^{-85}	0.022	−0.46	−0.42	−0.38
	Normal Velocity	8.44×10^{-18}	0.015	0.099	0.13	0.16
	Z-axis	0.0075	0.005	−0.023	−0.013	−0.0035
	Normal Velocity × Z-axis	0.0057	0.0010	0.00082	0.0028	0.0048
	X-axis × Z-axis	0.0010	0.00038	−0.0020	−0.0012	−0.00051
Specificity	**Type of impact ***	2.80×10^{-95}	0.016	0.31	0.34	0.37
	Normal Velocity	7.29×10^{-16}	0.012	−0.12	−0.10	−0.073
	X-axis × Z-axis	3.49×10^{-5}	0.00029	0.00062	0.0012	0.0017
Precision	**Type of impact ***	6.20×10^{-13}	0.0053	0.028	0.038	0.048
	Z-axis	1.50×10^{-7}	0.0014	−0.010	−0.0073	−0.0046
	Normal Velocity × Z-axis	1.15×10^{-5}	0.00024	0.00058	0.0010	0.0015
	Normal Velocity × X-axis	0.036	0.00065	8.85×10^{-5}	0.0014	0.0027

* Windshield: positive value and ground: negative value.

Appendix E

Finite Element to Imaging Data Transformation Pipeline

A pipeline was developed to convert finite element (FE) simulation results into data compatible with image analysis, in order to establish a link between clinical data and biomechanical tools. The aim is to integrate biomechanical data in clinical tools to improve lesion detection and care. Clinical diagnostic methods can then be applied to determine the similarity between biomechanical and clinical data. To enable the superimposition of FE simulation results with imaging data, a rigid body transformation is applied to align the FE model with the reference frame of the imaging dataset (Figure A3). This homogeneous transformation is represented by a matrix composed $T \in R^{4\times4}$ of a position matrix $R \in SO(3)$ and a translation vector $t \in R^3$:

$$T = \begin{bmatrix} R & t \\ 0 & 1 \end{bmatrix}$$

$$x' = Rx + t$$

Positions are applied sequentially in the order provided (around the X, Y, and Z axes, in degrees), followed by a translation in the same coordinate frame. This transformation ensures spatial consistency between the mechanical model and the imaging space. Simulation results are extracted for each element (e) and each time point (t). The maximal value of the maximum principal strain $\varepsilon_{max} = (t, e)$ are computed(Figure A3).

For the principal strain tensor $\varepsilon_i (i = 1, ..., 3)$, the maximum absolute principal strain is defined as:

$$\varepsilon_{max}(t, e) = max_i|\varepsilon_i|$$

Time series of strain values are aggregated per element to compute synthetic indicators:

$$\Sigma_\sigma(e) = \sum_t \sigma_{vm}(t, e) \text{and } \Sigma_\varepsilon(e) = \sum_t \varepsilon_{max}(t, e)$$

For visualization and analysis purposes, element-wise values are interpolated onto a regular three-dimensional grid (Figure A3) to produce volumes in NIFTI format (.nii.gz) (Figure A3).

$$V_{(x,y,z)} = \frac{1}{N_{el}} \sum_{e \epsilon voxel} Q(e)$$

where Q(e) denotes the interpolated quantity (e.g., strain).

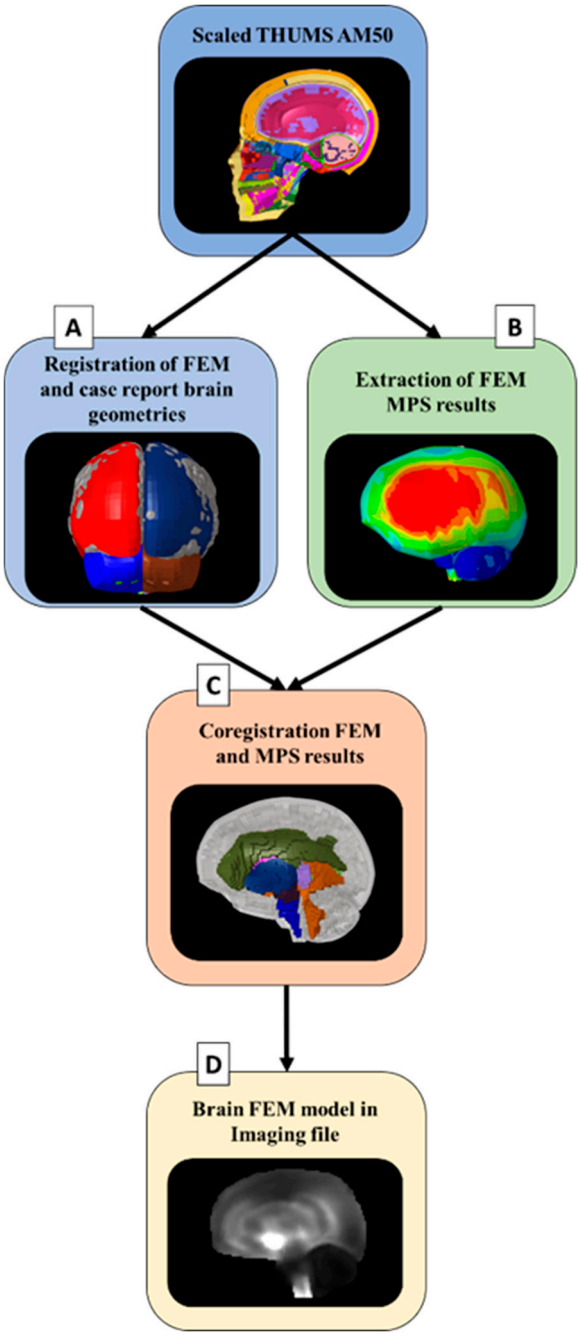

Figure A3. Diagram of the pipeline for the conversion of the FEM in imaging responses. (**A**) Registration of the FEM and case-report brain geometries, with different colors distinguishing anatomical regions used for alignment. (**B**) Extraction of maximum principal strain (MPS) results from the FEM, with colors representing strain magnitude, ranging from lower values (blue) to higher values (red). (**C**) Coregistration of the FEM geometry and MPS results with the case-report brain anatomy, with different colors identifying the mapped anatomical regions. (**D**) Conversion of the registered brain FEM model into an imaging file, displayed in grayscale for visualization in imaging space.

Appendix F

Sensibility Analysis of the MPS Injury Threshold

The sensitivity of the reconstructed scenario ranking to the selected injury threshold was assessed in analysis 2 using alternative thresholds reported in the literature

(0.18, 0.21 and 0.26) [74,75]. MCC values obtained with the 0.20 threshold were strongly correlated with those obtained using thresholds of 0.21 ($R^2 = 0.98$), 0.18 ($R^2 = 0.90$) and 0.26 ($R^2 = 0.79$). The ten best-performing simulations identified using the 0.20 threshold consistently ranked among the top twenty simulations across all three alternative thresholds.

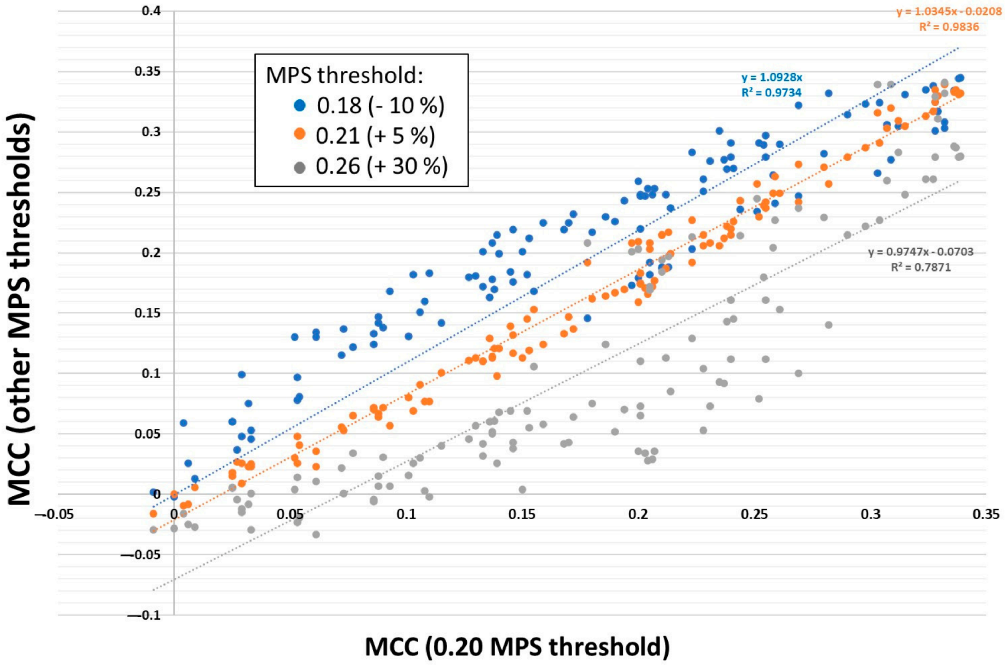

Figure A4. Sensitivity analysis of MCC results to the MPS threshold in analysis 2. MCC values obtained from the 120 simulations using MPS thresholds of 0.18 (blue), 0.21 (orange) and 0.26 (grey) are plotted as a function of the MCC values initially obtained using the 0.20 threshold. Dotted lines represent the corresponding linear regressions, with equations and R^2 values reported on the graph.

References

1. Evans, J.A.; van Wessem, K.J.P.; McDougall, D.; Lee, K.A.; Lyons, T.; Balogh, Z.J. Epidemiology of Traumatic Deaths: Comprehensive Population-Based Assessment. *World J. Surg.* **2010**, *34*, 158–163. [CrossRef] [PubMed]
2. Zetterberg, H.; Winblad, B.; Bernick, C.; Yaffe, K.; Majdan, M.; Johansson, G.; Newcombe, V.; Nyberg, L.; Sharp, D.; Tenovuo, O.; et al. Head Trauma in Sports—Clinical Characteristics, Epidemiology and Biomarkers. *J. Intern. Med.* **2019**, *285*, 624–634. [CrossRef] [PubMed]
3. Elkin, B.S.; Gabler, L.F.; Panzer, M.B.; Siegmund, G.P. Brain Tissue Strains Vary with Head Impact Location: A Possible Explanation for Increased Concussion Risk in Struck versus Striking Football Players. *Clin. Biomech.* **2019**, *64*, 49–57. [CrossRef] [PubMed]
4. Tan, X.G.; Sajja, V.S.S.S.; D'Souza, M.M.; Gupta, R.K.; Long, J.B.; Singh, A.K.; Bagchi, A. A Methodology to Compare Biomechanical Simulations With Clinical Brain Imaging Analysis Utilizing Two Blunt Impact Cases. *Front. Bioeng. Biotechnol.* **2021**, *9*, 654677. [CrossRef] [PubMed]
5. Simeone, P.; Auzias, G.; Lefevre, J.; Takerkart, S.; Coulon, O.; Lesimple, B.; Torkomian, G.; Battisti, V.; Jacquens, A.; Couret, D.; et al. Long-Term Follow-up of Neurodegenerative Phenomenon in Severe Traumatic Brain Injury Using MRI. *Ann. Phys. Rehabil. Med.* **2022**, *65*, 101599. [CrossRef] [PubMed]
6. Fischer, D.; Edlow, B.L. Coma Prognostication After Acute Brain Injury: A Review. *JAMA Neurol.* **2024**, *81*, 405–415. [CrossRef] [PubMed]
7. Yang, B.; Tse, K.-M.; Chen, N.; Tan, L.-B.; Zheng, Q.-Q.; Yang, H.-M.; Hu, M.; Pan, G.; Lee, H.-P. Development of a Finite Element Head Model for the Study of Impact Head Injury. *BioMed Res. Int.* **2014**, *2014*, 408278. [CrossRef] [PubMed]
8. Pavan, P.G.; Nasim, M.; Brasco, V.; Spadoni, S.; Paoloni, F.; d'Avella, D.; Khosroshahi, S.F.; de Cesare, N.; Gupta, K.; Galvanetto, U. Development of Detailed Finite Element Models for in Silico Analyses of Brain Impact Dynamics. *Comput. Methods Programs Biomed.* **2022**, *227*, 107225. [CrossRef] [PubMed]
9. Giordano, C.; Kleiven, S. Evaluation of Axonal Strain as a Predictor for Mild Traumatic Brain Injuries Using Finite Element Modeling. *Stapp Car Crash J.* **2014**, *58*, 29–62. [CrossRef] [PubMed]

10. Franklyn, M.; Fildes, B.; Zhang, L.; Yang, K.; Sparke, L. Analysis of Finite Element Models for Head Injury Investigation: Reconstruction of Four Real-World Impacts. *Stapp Car Crash J.* **2005**, *49*, 1–32. [CrossRef] [PubMed]
11. Rezek, C.; Godio-Raboutet, Y.; Llari, M.; Tuchtan, L.; Capuani, C.; Boval, C.; Piercecchi, M.-D.; Thollon, L.; Delteil, C. Forensic Analysis of Head Traumas: Can Biomechanics Shed Light?—A Case Report. *Diagnostics* **2026**, *16*, 766. [CrossRef] [PubMed]
12. Fahlstedt, M.; Depreitere, B.; Halldin, P.; Vander Sloten, J.; Kleiven, S. Correlation between Injury Pattern and Finite Element Analysis in Biomechanical Reconstructions of Traumatic Brain Injuries. *J. Biomech.* **2015**, *48*, 1331–1335. [CrossRef] [PubMed]
13. Bolcos, P.O.; Mononen, M.E.; Roach, K.E.; Tanaka, M.S.; Suomalainen, J.-S.; Mikkonen, S.; Nissi, M.J.; Töyräs, J.; Link, T.M.; Souza, R.B.; et al. Subject-Specific Biomechanical Analysis to Estimate Locations Susceptible to Osteoarthritis—Finite Element Modeling and MRI Follow-up of ACL Reconstructed Patients. *J. Orthop. Res.* **2022**, *40*, 1744–1755. [CrossRef] [PubMed]
14. Deng, X.; Du, Z.; Feng, H.; Wang, S.; Luo, H.; Liu, Y. Investigation on the Modeling and Reconstruction of Head Injury Accident Using ABAQUS/Explicit. *Bioengineering* **2022**, *9*, 723. [CrossRef] [PubMed]
15. Zhao, W.; Choate, B.; Ji, S. Material Properties of the Brain in Injury-Relevant Conditions—Experiments and Computational Modeling. *J. Mech. Behav. Biomed. Mater.* **2018**, *80*, 222–234. [CrossRef] [PubMed]
16. Tuchtan, L.; Piercecchi-Marti, M.-D.; Bartoli, C.; Boisclair, D.; Adalian, P.; Léonetti, G.; Behr, M.; Thollon, L. Forces Transmission to the Skull in Case of Mandibular Impact. *Forensic Sci. Int.* **2015**, *252*, 22–28. [CrossRef] [PubMed]
17. Tuchtan, L.; Godio-Raboutet, Y.; Delteil, C.; Léonetti, G.; Piercecchi Marti, M.-D.; Thollon, L. Study of Cerebrospinal Injuries by Force Transmission Secondary to Mandibular Impacts Using a Finite Element Model. *Forensic Sci. Int.* **2020**, *307*, 110118. [CrossRef] [PubMed]
18. Nahum, A.M.; Smith, R.; Ward, C.C. *Intracranial Pressure Dynamics During Head Impact*; SAE International: Warrendale, PA, USA, 1977.
19. Hardy, W.; Foster, C.; Mason, M.; Yang, K.; King, A.; Tashman, S. Investigation of Head Injury Mechanisms Using Neutral Density Technology and High-Speed Biplanar X-Ray. *Stapp Car Crash J.* **2001**, *45*, 337–368. [CrossRef] [PubMed]
20. Alshareef, A.; Wu, T.; Giudice, J.S.; Panzer, M.B. Toward Subject-Specific Evaluation: Methods of Evaluating Finite Element Brain Models Using Experimental High-Rate Rotational Brain Motion. *Biomech. Model. Mechanobiol.* **2021**, *20*, 2301–2317. [CrossRef] [PubMed]
21. Upadhyay, K.; Jagani, R.; Giovanis, D.G.; Alshareef, A.; Knutsen, A.K.; Johnson, C.L.; Carass, A.; Bayly, P.V.; Shields, M.D.; Ramesh, K.T. Effect of Human Head Shape on the Risk of Traumatic Brain Injury: A Gaussian Process Regression-Based Machine Learning Approach. *Mil. Med.* **2024**, *189*, 608–617. [CrossRef] [PubMed]
22. Zhang, Y.; Tang, L.; Liu, Y.; Yang, B.; Jiang, Z.; Liu, Z.; Zhou, L. An Objective Injury Threshold for the Maximum Principal Strain Criterion for Brain Tissue in the Finite Element Head Model and Its Application. *Bioengineering* **2024**, *11*, 918. [CrossRef] [PubMed]
23. Yuan, Q.; Li, X.; Zhou, Z.; Kleiven, S. A Novel Framework for Video-Informed Reconstructions of Sports Accidents: A Case Study Correlating Brain Injury Pattern from Multimodal Neuroimaging with Finite Element Analysis. *Brain Multiphys.* **2024**, *6*, 100085. [CrossRef]
24. Cardoso, C.G.S.; Salgado, A.A.; Fernandes, F.A.O.; de Sousa, R.J.A. Evaluating Brain Injury Outcomes in Female Subjects: A Computational Approach to Accident Reconstruction of Fatal and Non-Fatal Cases. *Injury* **2025**, *56*, 112164. [CrossRef] [PubMed]
25. Peng, Y.; Yang, J.; Deck, C.; Otte, D.; Willinger, R. Development of Head Injury Risk Functions Based on Real-World Accident Reconstruction. *Int. J. Crashworthiness* **2014**, *19*, 105–114. [CrossRef]
26. Wang, F.; Wang, Z.; Hu, L.; Xu, H.; Yu, C.; Li, F. Evaluation of Head Injury Criteria for Injury Prediction Effectiveness: Computational Reconstruction of Real-World Vulnerable Road User Impact Accidents. *Front. Bioeng. Biotechnol.* **2021**, *9*, 677982. [CrossRef] [PubMed]
27. Thollon, L.; Llari, M.; André, L.; Adalian, P.; Leonetti, G.; Piercecchi-Marti, M.-D. Biomechanical Analysis of Skull Fractures after Uncontrolled Hanging Release. *Forensic Sci. Int.* **2013**, *233*, 220–229. [CrossRef] [PubMed]
28. Henningsen, M.J.; Lindgren, N.; Kleiven, S.; Li, X.; Jacobsen, C.; Villa, C. Subject-Specific Finite Element Head Models for Skull Fracture Evaluation—A New Tool in Forensic Pathology. *Int. J. Leg. Med.* **2024**, *138*, 1447–1458. [CrossRef] [PubMed]
29. Wei, Y.; Oldroyd, J.; Haste, P.; Jayamohan, J.; Jones, M.; Casey, N.; Peña, J.-M.; Baylis, S.; Gilmour, S.; Jérusalem, A. A Mechanics-Informed Machine Learning Framework for Traumatic Brain Injury Prediction in Police and Forensic Investigations. *Commun. Eng.* **2025**, *4*, 29. [CrossRef] [PubMed]
30. Avignon, T.; Doat-Sarfati, V.; Agripnidis, T.; Cammilleri, Z.; Hak, J.-F.; Nakache, J.; Meunier, D.; Sein, J.; Goutal-Guérin, Y.; Morel, J.; et al. Prognostic Value of MRI Anatomical Radiologic Scores for One-Year Neurological Outcome After Severe Traumatic Brain Injury. *Neurocrit. Care* **2026**, *45*, 304–313. [CrossRef] [PubMed]
31. Dale, A.M.; Fischl, B.; Sereno, M.I. Cortical Surface-Based Analysis: I. Segmentation and Surface Reconstruction. *NeuroImage* **1999**, *9*, 179–194. [CrossRef] [PubMed]

32. Fischl, B.; Sereno, M.I.; Dale, A.M. Cortical Surface-Based Analysis: II: Inflation, Flattening, and a Surface-Based Coordinate System. *NeuroImage* **1999**, *9*, 195–207. [CrossRef] [PubMed]
33. Reuter, M.; Schmansky, N.J.; Rosas, H.D.; Fischl, B. Within-Subject Template Estimation for Unbiased Longitudinal Image Analysis. *NeuroImage* **2012**, *61*, 1402–1418. [CrossRef] [PubMed]
34. Reuter, M.; Rosas, H.D.; Fischl, B. Highly Accurate Inverse Consistent Registration: A Robust Approach. *NeuroImage* **2010**, *53*, 1181–1196. [CrossRef] [PubMed]
35. Cole, J.H.; Jolly, A.; De Simoni, S.; Bourke, N.; Patel, M.C.; Scott, G.; Sharp, D.J. Spatial Patterns of Progressive Brain Volume Loss after Moderate-Severe Traumatic Brain Injury. *Brain* **2018**, *141*, 822–836. [CrossRef] [PubMed]
36. Donat, C.K.; Yanez Lopez, M.; Sastre, M.; Baxan, N.; Goldfinger, M.; Seeamber, R.; Müller, F.; Davies, P.; Hellyer, P.; Siegkas, P.; et al. From Biomechanics to Pathology: Predicting Axonal Injury from Patterns of Strain after Traumatic Brain Injury. *Brain* **2021**, *144*, 70–91. [CrossRef] [PubMed]
37. Yang, S.; Tang, J.; Nie, B.; Zhou, Q. Assessment of Brain Injury Characterization and Influence of Modeling Approaches. *Sci. Rep.* **2022**, *12*, 13597. [CrossRef] [PubMed]
38. Iwamoto, M.; Omori, K.; Kimpara, H.; Nakahira, Y.; Tamura, A.; Watanabe, I.; Miki, K.; Hasegawa, J.; Oshita, F. Recent Advances in THUMS: Development of Individual Internal Organs, Brain. In Proceedings of the 4th European LS-DYNA Users Conference (C–I-01 2003), Ulm, Germany, 22–23 May 2003.
39. Paas, R.; Davidsson, J.; Brolin, K. Head Kinematics and Shoulder Biomechanics in Shoulder Impacts Similar to Pedestrian Crashes—A THUMS Study. *Traffic Inj. Prev.* **2015**, *16*, 498–506. [CrossRef] [PubMed]
40. Bouvette, V.; Guay, S.; De Beaumont, L.; Petit, Y.; Vinet, S.-A.; Wagnac, E. Role of Player-Specific White Matter Parcellation and Scaling in Impact-Induced Strain Responses. *Biomech. Model. Mechanobiol.* **2025**, *24*, 939–961. [CrossRef] [PubMed]
41. Li, X.; Zhou, Z.; Kleiven, S. An Anatomically Detailed and Personalizable Head Injury Model: Significance of Brain and White Matter Tract Morphological Variability on Strain. *Biomech. Model. Mechanobiol.* **2021**, *20*, 403–431. [CrossRef] [PubMed]
42. Wu, S.; Zhao, W.; Wu, Z.; McAllister, T.; Hu, J.; Ji, S. Approximating Subject-Specific Brain Injury Models via Scaling Based on Head–Brain Morphological Relationships. *Biomech. Model. Mechanobiol.* **2023**, *22*, 159–175. [CrossRef] [PubMed]
43. Crocetta, G.; Piantini, S.; Pierini, M.; Simms, C. The Influence of Vehicle Front-End Design on Pedestrian Ground Impact. *Accid. Anal. Prev.* **2015**, *79*, 56–69. [CrossRef] [PubMed]
44. Gao, W.; Zhao, G.; He, X.; Chen, S.; Wang, C. A High-Fidelity Numerical Approach for Dummy Head-Windshield Contact Interactions. *Int. J. Impact Eng.* **2023**, *176*, 104560. [CrossRef]
45. Reichert, R.; Park, C.-K.; Morgan, R.M. *Development of Integrated Vehicle-Occupant Model for Crashworthiness Safety Analysis*; Report No. DOT HS 812 087; National Highway Traffic Safety Administration: Washington, DC, USA, 2014. Available online: https://www.nhtsa.gov/sites/nhtsa.gov/files/documents/812087_ivomforcrashworthiness.pdf (accessed on 6 October 2025).
46. Luque, A.; Carrasco, A.; Martín, A.; de las Heras, A. The Impact of Class Imbalance in Classification Performance Metrics Based on the Binary Confusion Matrix. *Pattern Recognit.* **2019**, *91*, 216–231. [CrossRef]
47. Obi, J.C. A Comparative Study of Several Classification Metrics and Their Performances on Data. *World J. Adv. Eng. Technol. Sci.* **2023**, *8*, 308–314. [CrossRef]
48. Restrepo, F.; Mali, N.; Abrahams, A.; Ractham, P. Formal Definition of the MARS Method for Quantifying the Unique Target Class Discoveries of Selected Machine Classifiers. *F1000Research* **2022**, *11*, 391. [CrossRef]
49. Sujon, K.M.; Hassan, R.; Choi, K.; Samad, M.A. Accuracy, Precision, Recall, F1-Score, or MCC? Empirical Evidence from Advanced Statistics, ML, and XAI for Evaluating Business Predictive Models. *J. Big Data* **2025**, *12*, 268. [CrossRef]
50. Chicco, D.; Jurman, G. The Matthews Correlation Coefficient (MCC) Should Replace the ROC AUC as the Standard Metric for Assessing Binary Classification. *BioData Min.* **2023**, *16*, 4. [CrossRef] [PubMed]
51. Cao, C.; Chicco, D.; Hoffman, M.M. The MCC-F1 Curve: A Performance Evaluation Technique for Binary Classification 2020. *arXiv* **2020**, arXiv:2006.11278.
52. Ruiz-de-León, G.; Baus-Domínguez, M.; González-Martín, M.; Gutiérrez-Corrales, A.; Torres-Carranza, E.; Martínez-González, Á.-J.; Torres-Lagares, D.; López-Millán, J.; Ambrosiani-Fernández, J. Study of the Impact on Zygomatic Bone Using Numerical Simulation. *Biomimetics* **2024**, *9*, 696. [CrossRef] [PubMed]
53. Sahoo, D.; Deck, C.; Willinger, R. Brain Injury Tolerance Limit Based on Computation of Axonal Strain. *Accid. Anal. Prev.* **2016**, *92*, 53–70. [CrossRef] [PubMed]
54. Motherway, J.A.; Doorly, M.C.; Curtis, M.; Gilchrist, M.D. Head Impact Biomechanics Simulations: A Forensic Tool for Reconstructing Head Injury? *Leg. Med.* **2009**, *11*, 220–222. [CrossRef] [PubMed]
55. Jolly, A.E.; Bălăeţ, M.; Azor, A.; Friedland, D.; Sandrone, S.; Graham, N.S.N.; Zimmerman, K.; Sharp, D. Detecting Axonal Injury in Individual Patients after Traumatic Brain Injury. *Brain* **2020**, *144*, 92–113. [CrossRef] [PubMed]
56. Andreasen, S.H.; Andersen, K.W.; Conde, V.; Dyrby, T.B.; Puonti, O.; Kammersgaard, L.P.; Madsen, C.G.; Madsen, K.H.; Poulsen, I.; Siebner, H.R. Limited Colocalization of Microbleeds and Microstructural Changes after Severe Traumatic Brain Injury. *J. Neurotrauma* **2020**, *37*, 581–592. [CrossRef] [PubMed]

57. Graham, N.S.N.; Jolly, A.E.; Zimmerman, K.; Bourke, N.; Scott, G.; Cole, J.; Schott, J.; Sharp, D. Diffuse Axonal Injury Predicts Neurodegeneration after Moderate-Severe Traumatic Brain Injury. *Brain* **2020**, *143*, 3685–3698. [CrossRef] [PubMed]
58. Zhao, W.; Ji, S. Cerebral Vascular Strains in Dynamic Head Impact Using an Upgraded Model with Brain Material Property Heterogeneity. *J. Mech. Behav. Biomed. Mater.* **2022**, *126*, 104967. [CrossRef] [PubMed]
59. Tu, T.-W.; Williams, R.A.; Lescher, J.D.; Jikaria, N.; Turtzo, L.C.; Frank, J.A. Radiological–Pathological Correlation of Diffusion Tensor and Magnetization Transfer Imaging in a Closed Head Traumatic Brain Injury Model. *Ann. Neurol.* **2016**, *79*, 907–920. [CrossRef] [PubMed]
60. Budde, M.D.; Janes, L.; Gold, E.; Turtzo, L.C.; Frank, J.A. The Contribution of Gliosis to Diffusion Tensor Anisotropy and Tractography Following Traumatic Brain Injury: Validation in the Rat Using Fourier Analysis of Stained Tissue Sections. *Brain* **2011**, *134*, 2248–2260. [CrossRef] [PubMed]
61. Zhao, W.; Ji, S. White Matter Anisotropy for Impact Simulation and Response Sampling in Traumatic Brain Injury. *J. Neurotrauma* **2019**, *36*, 250–263. [CrossRef] [PubMed]
62. Tayebi, M.; Kwon, E.E.; Maller, J.; McGeown, J.; Scadeng, M.; Qiao, M.; Wang, A.; Nielsen, P.; Fernandez, J.; Holdsworth, S.; et al. Integration of Diffusion Tensor Imaging Parameters with Mesh Morphing for In-Depth Analysis of Brain White Matter Fibre Tracts. *Brain Commun.* **2024**, *6*, fcae027. [CrossRef] [PubMed]
63. Deck, C.; Willinger, R. Improved Head Injury Criteria Based on Head FE Model. *Int. J. Crashworthiness* **2008**, *13*, 667–678. [CrossRef]
64. Lee, W.; Kim, T.-S. Methods for High-Resolution Anisotropic Finite Element Modeling of the Human Head: Automatic MR White Matter Anisotropy-Adaptive Mesh Generation. *Med. Eng. Phys.* **2011**, *34*, 85–98. [CrossRef] [PubMed]
65. Hoursan, H.; Farahmand, F.; Ahmadian, M. Effect of Axonal Fiber Architecture on Mechanical Heterogeneity of the White Matter—A Statistical Micromechanical Model. *Comput. Methods Biomech. Biomed. Eng.* **2021**, *25*, 27–39. [CrossRef] [PubMed]
66. McAllister, T.W.; Ford, J.C.; Ji, S.; Beckwith, J.G.; Flashman, L.A.; Paulsen, K.; Greenwald, R.M. Maximum Principal Strain and Strain Rate Associated with Concussion Diagnosis Correlates with Changes in Corpus Callosum White Matter Indices. *Ann. Biomed. Eng.* **2012**, *40*, 127–140. [CrossRef] [PubMed]
67. Rampp, S.; Budday, S.; Reiter, N.; Tueni, N.; Hinrichsen, J.; Bräuer, L.; Paulsen, F.; Schnell, O.; Flé, G.; Laun, F.B.; et al. Fractional Anisotropy as a Surrogate Marker of Brain Mechanics. *bioRxiv* **2026**. [CrossRef]
68. Delteil, C.; Manlius, T.; Marle, O.; Godio-Raboutet, Y.; Bailly, N.; Piercecchi-Marti, M.-D.; Tuchtan, L.; Thollon, L. Head Injury: Importance of the Deep Brain Nuclei in Force Transmission to the Brain. *Forensic Sci. Int.* **2024**, *356*, 111952. [CrossRef] [PubMed]
69. Shim, V.B.; Tayebi, M.; Kwon, E.E.; Guild, S.; Scadeng, M.; Dubowitz, D.; McBryde, F.; Rosset, S.; Wang, A.; Fernandez, J.W.; et al. Combining Advanced Magnetic Resonance Imaging (MRI) with Finite Element (FE) Analysis for Characterising Subject-Specific Injury Patterns in the Brain after Traumatic Brain Injury. *Eng. Comput.* **2022**, *38*, 3925–3937. [CrossRef]
70. Sahoo, D.; Marini, G. Improvement and Validation of THUMSv4.1 AM50 Face Model in Virtual Performance Solution and Development of Model Specific Facial Fracture Criteria. In Proceedings of the IRCOBI Conference 2026 (IRC-26-121 2026), Munich, Germany, 9 September 2026. Available online: https://www.ircobi.org/wordpress/downloads/irc26/pdf-files/26121.pdf (accessed on 6 October 2025).
71. Ghajari, M.; Peldschus, S.; Galvanetto, U.; Iannucci, L. Effects of the Presence of the Body in Helmet Oblique Impacts. *Accid. Anal. Prev.* **2013**, *50*, 263–271. [CrossRef] [PubMed]
72. Rycman, A.; McLachlin, S.; Cronin, D.S. A Hyper-Viscoelastic Continuum-Level Finite Element Model of the Spinal Cord Assessed for Transverse Indentation and Impact Loading. *Front. Bioeng. Biotechnol.* **2021**, *9*, 693120. [CrossRef] [PubMed]
73. Giudice, J.S.; Alshareef, A.; Wu, T.; Knutsen, A.K.; Hiscox, L.V.; Johnson, C.L.; Panzer, M.B. Calibration of a Heterogeneous Brain Model Using a Subject-Specific Inverse Finite Element Approach. *Front. Bioeng. Biotechnol.* **2021**, *9*, 664268. [CrossRef] [PubMed]
74. Bain, A.C.; Meaney, D.F. Tissue-Level Thresholds for Axonal Damage in an Experimental Model of Central Nervous System White Matter Injury. *J. Biomech. Eng.* **2000**, *122*, 615–622. [CrossRef] [PubMed]
75. Kleiven, S. Predictors for Traumatic Brain Injuries Evaluated through Accident Reconstructions. *Stapp Car Crash J.* **2007**, *51*, 81–114. [CrossRef] [PubMed]

Disclaimer/Publisher's Note: The statements, opinions and data contained in all publications are solely those of the individual author(s) and contributor(s) and not of MDPI and/or the editor(s). MDPI and/or the editor(s) disclaim responsibility for any injury to people or property resulting from any ideas, methods, instructions or products referred to in the content.